Beating spectral bandwidth limits for large aperture broadband nano-optics

Johannes E. Fröch [1,2,8] ✉, Praneeth Chakravarthula [3,8], Jipeng Sun[4], Ethan Tseng [4], Shane Colburn[2], Alan Zhan[5], Forrest Miller[2], Anna Wirth-Singh[1], Quentin A. A. Tanguy [2], Zheyi Han[2], Karl F. Böhringer [2,6,7], Felix Heide [4] & Arka Majumdar [1,2] ✉

Flat optics have been proposed as an attractive approach for the implementation of new imaging and sensing modalities to replace and augment refractive optics. However, chromatic aberrations impose fundamental limitations on diffractive flat optics. As such, true broadband high-quality imaging has thus far been out of reach for fast f-numbers, large aperture, flat optics. In this work, we overcome intrinsic spectral bandwidth limitations, achieving broadband imaging in the visible wavelength range with a flat meta-optic, co-designed with computational reconstruction. We derive the necessary conditions for a broadband, 1 cm aperture, f/2 flat optic, with a diagonal field of view of 30° and average system MTF contrast of 20% or larger for a spatial frequency of 100 lp/mm in the visible band (>30% for <70 lp/mm). Finally, we use a coaxial, dual-aperture system to train the broadband imaging meta-optic with a learned reconstruction method operating on pair-wise captured imaging data. Fundamentally, our work challenges the entrenched belief of the inability of capturing high-quality, full-color images using a single large aperture meta-optic.

Cameras have become omnipresent in our contemporary life as integral parts in laptops, smartphones, automotive sensors, medical instruments, and surveillance[1–3]. While novel image processing methods achieve progressively higher definitions and extract increasingly more information, miniaturization of optical elements has become equally, if not a more important challenge for emerging applications. For instance, smaller lenses could facilitate less invasive surgeries with optical endoscopes, lightweight systems could reduce the power consumption of airborne drones and satellites, and even the lens bump in mobile phone cameras, ultimately limiting the thickness of smartphones, could be eliminated.

To this end, flat diffractive optics promise to replace or augment refractive lenses in these scenarios. Specifically, meta-optics - sub-

wavelength, diffractive, quasi-periodic arrays of nano-scale scatterers, can alter the transmitted wavefront by locally imparting a desired phase delay. Given this designer potential[4–7], an emerging body of work has explored exotic functionalities, such as holography[8–10], multi-modal sensing applications[11–17], spectrometers and hyperspectral imagers[18–21], or optical encoders for hybrid neural networks[22–26].

Diffractive optics, however, have fundamental limitations. To reduce the thickness, the absolute phase is wrapped to a range of (typically) $0 - 2\pi$, which introduces chromatic aberrations that are significantly larger than those of refractive lenses[27,28]. While one can design a meta-optic that achieves a diffraction-limited point spread function (PSF) for a specific wavelength, it will perform poorly over an extended bandwidth at the same focal length. For large apertures

[1]Department of Physics, University of Washington, Seattle, WA, USA. [2]Department of Electrical and Computer Engineering, University of Washington, Seattle, WA, USA. [3]Department of Computer Science, University of North Carolina at Chapel Hill, Chapel Hill, USA. [4]Department of Computer Science, Princeton University, Princeton, NJ, USA. [5]Tunoptix, 4000 Mason Road 300, Fluke Hall, Seattle, WA, USA. [6]Department of Bioengineering, University of Washington, Seattle, WA, USA. [7]Institute for Nano-Engineered Systems, University of Washington, Seattle, WA, USA. [8]These authors contributed equally: Johannes E. Fröch, Praneeth Chakravarthula. ✉e-mail: jfroech@uw.edu; arka@uw.edu

and larger numerical apertures (NA), it is fundamentally not possible to obtain high performance of the standalone meta-optic over a broad spectral bandwidth and useful NA, as detailed in several works[29,30]. This has thus far restricted broadband meta-optics to either small apertures (~ 100 μm), low NAs (~ 0.05), or strongly limited resolution[31–36].

To overcome this fundamental limitation, several efforts have investigated high-quality imaging by computational reconstruction[37–42]. Images captured by the meta-optic are passed to a computational back end, which improves the image quality through aberration correction. However, broadband, full-color imaging with a single meta-optic at a large aperture (> 4 mm), suitable for integration with consumer electronics, has been illusive thus far. Existing works that utilized computational post-processing also lacked an understanding of an intuitive appropriate design approach. We find that understanding why certain designs of meta-optics provide enhanced image quality and why these are more amenable for computational post-processing enables general functional meta-optics.

We demonstrate polarization-insensitive, full-color, broadband imaging under ambient visible light and arbitrary scenes, with a single large aperture (1 cm diameter, f/2 lens) meta-optic, suitable for camera integration. Thanks to the large aperture, we achieve video-rate exposure times at a full diagonal field of view of ~ 30°. Although the standalone meta-optic is not performing at the diffraction limit, the co-designed computational back-end augments aberration correction and facilitates high-quality imaging, on par with a single refractive lens of the same diameter and f-number. Even more strikingly, for large field angles and depth of field, the meta-optic outperforms the single refractive optic. We further leverage recent breakthroughs in computer science to reinforce the computational backend utilizing a probabilistic diffusion-based reconstruction method. We further implemented a dual-aperture configuration to train and verify a learned backend. Through this approach, we ultimately demonstrate

imaging quality comparable to that of current-generation compound smartphone lenses.

Results

Design challenges in large aperture broadband meta-optics

Thanks to sophisticated ray tracing software, the design and optimization of refractive lenses and optical assemblies are well established. In contrast, complex meta-optics typically require a form of full-wave simulation to accurately capture their diffractive nature and account for the sub-wavelength feature scale. This amounts to solving a computationally prohibitive problem: a single meta-optic with a scatterer spacing of ~ 250 nm, and 1 cm circular aperture requires the computation of ~ 10^9 scatterers (Fig. 1a), equal to ~ 7 GB of RAM to analyze their performance using the angular spectrum method. This number linearly increases with the sampling rate of wavelength and field. Although a single simulation for such a device is possible, optimization involves tens of thousands to achieve sufficient quality.

To overcome this challenge, we optimize a large aperture, broadband meta-optic in two consecutive steps, assuming a radially symmetric phase profile and propagation conditions, which reduces design parameters to ~ 10^4. Although this considers only on-axis field propagation, it is a reasonable constraint. First, as we demonstrate experimentally, emerging broadband designs have an extended depth of focus, which effectively counteracts the field curvature for the larger angle of incidence. Second, the radial symmetry of the lens ensures a symmetric PSF, reducing artefacts during computational reconstruction, which impeded previous designs. Third, radial symmetry presents the most generalized conditions for imaging and, hence, does not introduce any artefacts in certain directions over the implemented field of view. Thus, we ensure that such designs achieve spectral broadband and reasonable field angle, with uniform performance.

As outlined in Fig. 1b, we used a differentiable pipeline, which iteratively improves the phase profile to maximize the intensity of the
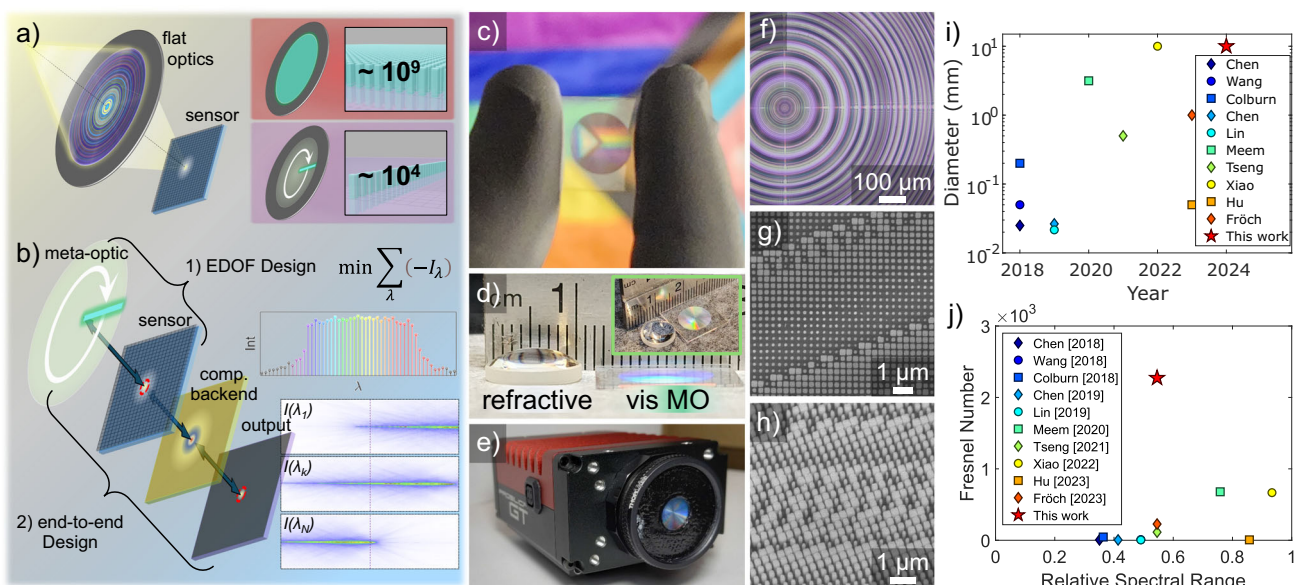
Fig. 1 | Design and fabrication of the large aperture full-color meta-optic. a Schematic description of the design challenge to achieve broadband focusing. By constraining the propagation to only the on-axis field, we compress the design space of required scatterers from ~ 10^9 to ~ 10^4. **b** The broadband capability is implemented in a two-step optimization process, where a meta-optic is first designed to exhibit maximal focal intensity for a dense sampling of wavelengths. Here, solely the intensity of the PSF for a broad spectral range at the center is maximized. This yields extended focus profiles along the optical axis as plotted for three different wavelengths, within the optimization set. In the second step, we use this phase profile as an initial condition for an end-to-end computational imaging

optimization approach. **c** Picture of the 1 cm aperture meta-optic held towards a vivid scene, illustrating the direct lensing behavior. **d** Side by side comparison of the meta-optic with a refractive lens of the same aperture and f-number. **e** The 1 cm aperture broadband meta-optic integrated with a camera using a 3D printed holder. **f** Optical microscope image of the center of the meta-optic. **g, h** show scanning electron microscope (SEM) images of the scatterer in a top view and oblique view of 30°. **i** Comparison of aperture size for broadband meta-optic[31–33,35–37,55,56] and multi-level diffractive[46,47]. **j** Comparison of the same works with respect to Fresnel number.

point spread function across a spectral range of 450 nm–650 nm, with a sampling rate of 0.1 nm (details in the Method). This technique exploits symmetry of the meta-optic as well as memory reduction associated with only needing to compute the intensity at focus, utilizing a TensorFlow implementation of the Rayleigh-Sommerfeld diffraction integral to optimize the meta-optic using automatic differentiation. This initial step yields an extended depth of field (EDOF) profile, featuring a focus profile that extends over a longer distance along the optical axis, as shown for 3 different wavelengths in Fig. 1b. Intuitively, we can understand the broadband functionality, due to the inverse dependence of focal length to wavelength, akin to the focal shift of a standard hyperboloid metalens[27,28]. As the focus profile extends over a longer depth for all wavelengths, a similar point spread function (PSF) is maintained in a common plane for all wavelengths in the broad spectral range, as shown in Fig. 1b.

While this initial design is already suitable for broadband imaging, we further improve the performance using an end-to-end co-optimization approach with a complementary physics-informed computational backend, utilizing a learned probabilistic prior-based reconstruction method (details in the Method). This step ensures that imaging is amenable for computational reconstruction. End-to-end design was performed for two specific applications; one to achieve high-quality imaging for 3 distinct wavelengths in the red, green, and blue range (i.e., a polychromatic design); the second one for broadband operation, with a sampling of ∼ 5 nm over the whole visible range. While the former could, for instance, be implemented in applications where the spectrum of the light source can be controlled (e.g., virtual reality visors), the latter is suitable for broadband imaging under ambient light conditions. Further results and discussion on the optimization are provided in the Supplementary Information. An image of the fabricated broadband meta-optic, held towards a vivid scene, is shown in Fig. 1c, illustrating the lensing capability, while preserving colors across the visible spectrum.

Meta-optic fabrication, integration, and characteristics

A side-by-side comparison with a refractive lens of the same aperture and f-number (Fig. 1d) highlights the size reduction. We note that the thickness of the meta-optic scatterer is on the order of 1 μm, thus demonstrating a thickness reduction of 4 orders of magnitude (considering the sagitta of the refractive lens). Importantly, we show that despite orders of magnitude reduction in size, parity in image quality is possible and can even outperform the refractive lens in some cases.

We integrated the flat nano-optics directly with a commercial camera (Allied Vision, ProSilica GT1930) using a 3D-printed aperture, shown in Fig. 1e. Without the aid of any relay optic, we can directly assess the imaging performance from a system-level perspective. Previously employed relay configurations, as often used in meta-optic works[32,33,37,40], required long exposure times due to their reduced NA relative to the meta-optic and the effective reduction in pixel size with the relay's associated magnification. In comparison, the large aperture size of the presented broadband meta-optic enables imaging at high framerates as the entire sensor is utilized without an NA-mismatched objective or extra magnifying optics in the path.

All presented meta-optics considered in this work were fabricated in a SiN-on-quartz platform, fully detailed in the methods section and Supplementary Information. The simple square scatterer geometry and material platform (SiN on quartz) are suitable for mass manufacturing in foundries using nanoimprint lithography, which is cost-effective and scalable. Notably, this is a clear advantage over complex scatterer geometries that are typically required to implement dispersion engineering approaches. This makes adaption for foundry processes particularly appealing, which have recently put forth significant effort to adopt meta-optics[43–45].

Importantly in our fabrication, we achieve uniform structural integrity over the entire 1 cm aperture, apparent as a radially equal structural color effect, seen in optical microscope images (Fig. 1f and Supplementary Information), and by direct inspection of the nanostructure in a Scanning Electron Microscope from top and oblique angles as shown in Figs. 1g, and 1h, respectively. Further details and characterization are presented in the Supplementary Information.

To assess the broadband meta-optic imaging capability achieved in this work relative to previous flat optics (including multi-layer diffractive), we have summarized a comparison of aperture sizes demonstrated over recent years in Fig. 1i, and plotted their Fresnel Number ($\frac{r^2}{f\lambda_0}$) against the relative spectral range ($\frac{\Delta\lambda}{\lambda_0}$) in Fig. 1j, where r is the radius of the aperture, f is the focal length, $\Delta\lambda$ is the spectral range and λ_0 is the center wavelength. While the Fresnel number is a good indicator for lens power, it becomes increasingly challenging to realize a lens that can operate over a large bandwidth and maintain a high Fresnel number. Notably, the present work demonstrates the largest meta-optic (i.e., nanostructure) for visible broadband imaging so far, whereas similarly large apertures[46,47] were only demonstrated using MLDs. Moreover, a comparison in the calculated Fresnel Number shows more than an order of magnitude larger value, even considering MLDs.

Performance benchmarking against a refractive lens

For a clear experimental demonstration of the broadband capability, we benchmarked all meta-optics against an equivalent refractive lens (Fig. 1d). Doing so, we make a fair head-to-head comparison between meta-optic and refractive lens (plano-convex lens, with the same f-number and aperture size) on the same sensor, thus considering scaling effects in lens aberrations, which are often otherwise neglected[48,49]. This establishes a clear insight of what constitutes the strong performance of the comprehensive end-to-end design in comparison to others, including the initial (hyperboloid metalens), intermediate (EDOF design), and end-to-end polychromatic.

First, we measured the PSF directly on the sensor for narrow linewidths over a broad spectral range and varying angles of incidences (aoi) from 0° to 15° in steps of 5°. As shown in Fig. 2a, light from a tunable source was collimated and focused by the meta-optic, forming the PSF, which was then directly captured on the sensor at the design focal length, which remained constant throughout the characterization. All measurements, including PSFs of other devices, are summarized in the Supplementary Information. Overall, we observe that throughout the experimentally accessible spectral range (480–680 nm) and for low aoi (0°, 5°), the refractive lens maintains a narrow PSF, which becomes strongly aberrated towards larger aoi (10°, 15°) (Fig. 2b). In comparison, the fully optimized broadband end-to-end design exhibits a slightly extended PSF at lower aoi but overall maintains a smaller size towards larger aoi (Fig. 2c). This feature arises from the EDOF-like behavior of the broadband design, as further detailed in the Supplementary Information. To quantitatively validate the performance, we measured line pair contrasts in the visible spectral range from 480 nm to 680 nm, in steps of 2 nm for all lenses. As illustrated in Fig. 2d, light from a continuous source, filtered to a specific wavelength, was passed through a diffuser and objective to provide spatial and directionally uniform illumination of a standard resolution target (USAF 1951), which was placed at a focal length in front of the optical element. We imaged elements of groups 7, 6, 5, and 4 to obtain line pair contrasts across a spatial frequency range from ∼ 10 lp/mm up to ∼ 150 lp/mm. Figure 2e, shows a representative image captured with the broadband meta-optic at 580 nm. We note that the non-uniform appearance of the image occurred due to speckle pattern formation from the diffuser. Importantly, this measurement gives direct insight into the performance enhancement once the computational backend is applied to the captured images (Fig. 2f).

Figure 2g directly compares the extracted line pair contrasts at a single wavelength for a refractive lens, a hyperboloid metalens, and the end-to-end broadband meta-optic, before and after computation.
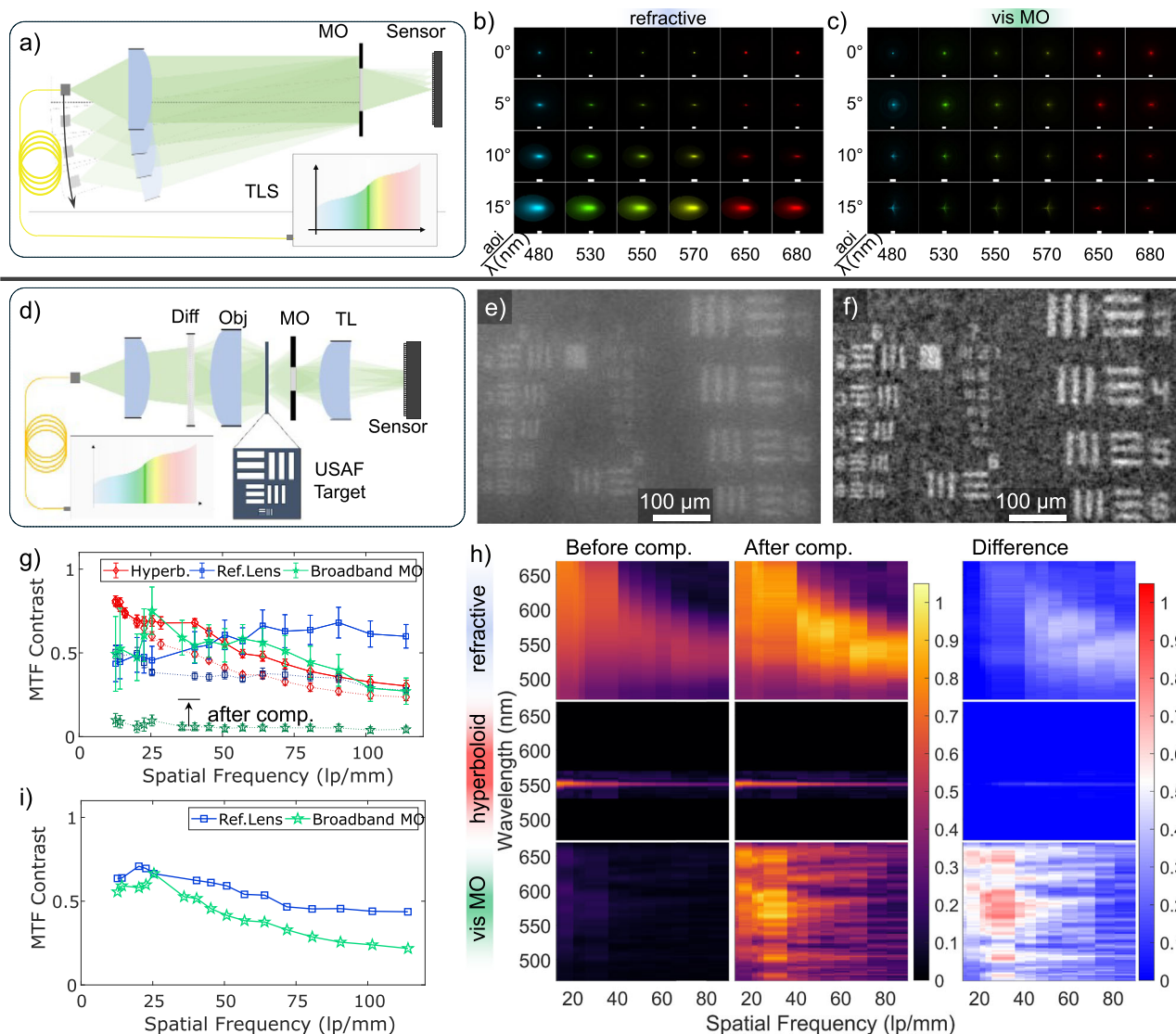
Fig. 2 | Measurement of meta-optic performance. a Schematic of the optical setup to measure the point spread function (PSF) for various optical elements under different angles of incidence (aoi). Comparison of measured PSFs for a plano-convex lens (**b**) and the broadband end-to-end meta-optic (**c**) for aoi of 0°, 5°,10°, and 15°. Scale bars in the images correspond to 40 μm for aoi of 0° and 5°, and 200 μm for aoi of 10° and 15°. **d** Schematic of the optical setup to measure the contrast values for various optical elements for different wavelengths. **e** 20 x magnified raw image of the USAF 1951 target with elements of groups 5, 6, and 7 captured with the broadband end-to-end designed meta-optic for a wavelength of 580 nm. **f** The same image after computational reconstruction is applied to the image. **g** Examples of enhancement in MTF for line pair contrast before (dashed lines) and after (full lines) deconvolution for the hyperboloid (red diamond), refractive (blue square), and end-to-end design (green star). The error bars represent one standard deviation of the average intensity. **h** Comparison of the obtained contrast values for line pairs are shown before (left column) and after deconvolution (middle column), as well as the relative difference (right column). From the top down, the plots correspond to the refractive lens, the hyperboloid metalens, and the end-to-end broadband meta-optic. **i** Average line pair contrast over the measured spectral range for the refractive lens in comparison to the broadband meta-optic.

Remarkably, the line pair contrast for the broadband meta-optic increased by a factor of ~ 6 after computation and reached values on par with the refractive lens. In comparison, the refractive lens, or hyperboloid lens, shows almost no increase after the computational backend.

Line pair contrasts across the entire spectral range for the different optics are plotted in Fig. 2h, as captured, after deconvolution, and their respective difference. Notably, the hyperboloid metalens perform on par with the refractive lens only over a very narrow spectral band (~ 10 nm), and improvement after computation is miniscule. Conversely, we observe that the broadband meta-optic lags in performance for raw imaging over the entire range. The designed point spread function features a strong peak component with a distributed tail, which, without reconstruction, appears as an aberrated component. However, as the peak component is preserved, the image contrast gains significantly after deconvolution with a value of > 40% across the broadband range for line-pair contrast of ~ 10 − 50 lp/mm, on par with the refractive lens. This finding validates the applicability for broadband, full-color imaging in consumer electronics, such as laptops, surveillance cameras, or smartphones, as image information in these scenarios is mostly contained in the lower spatial frequency range due to a high degree of sparsity in common scenes[50]. For instance, this is exploited for image compression or various state-of-the-art image enhancement algorithms in smartphones[2]. We note that some variations in plots appear due to varying positions of the target elements in the respective field of views.

Imaging performance with a physics based inverse filter
Overall, in comparison to other meta-optics, the broadband end-to-end design leverages the computational backend most efficiently to
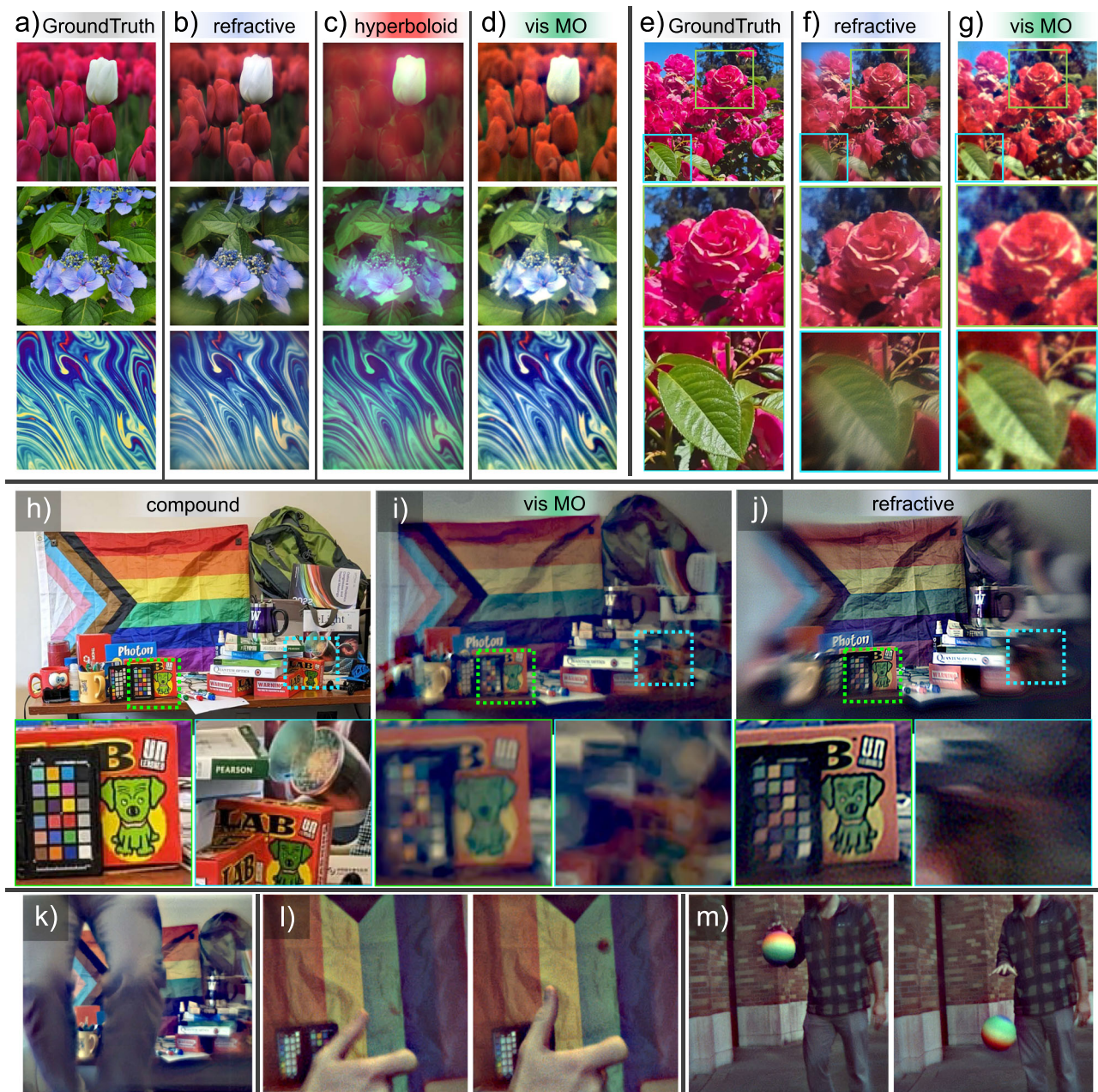
Fig. 3 | Meta-optic imaging and comparison to refractive optics. In the first row, a set of images was projected on an OLED screen, subsequently captured with various optical elements, and then reconstructed. To compare the design in the absence of learned priors, we employ here Wiener filtering as a physics-informed inverse filtering. Columns from left to right correspond to the ground truth (**a**), and the computationally reconstructed images with (**b**) refractive lens, (**c**) hyperboloid metalens, and (**d**) end-to-end designed meta-optic. Direct image comparison with details magnified of a ground truth image (**e**) for a refractive lens (**f**) and the end-to-end meta-optic (**g**). **h** Scene prepared for comparison for real-life-scenario broadband imaging (no display capture). Images captured of the scene are shown in (**i**) and (**j**) using the broadband meta-optic and a refractive lens, respectively. Parts of the scene at the center (green outline) and off-axis (blue outline) are magnified for better comparison of various details. **k** Single frames from a series capturing a person jumping in front of the scene shown in (**h**). **l** Frames showing a coin flip. **m** Frames of a person bouncing a colorful ball, captured outside under daylight conditions.

achieve high-quality imaging. This can be seen as a synergistic effect of the end-to-end design, where meta-optic and computational backend both contribute to improved imaging performance. Importantly, with the developed optimization process, we achieved a well-balanced PSF (and thus MTF), which exhibits similar performance over the entire spectral range (fully discussed in the Supplementary Information). While certain wavelengths perform better for other lenses, the broadband design achieves, on average the best performance and yields the largest improvement provided by the computational backend.

To demonstrate how these metrics translate to broadband imaging, we projected a series of full-color scenes on an OLED screen (details in Method) and captured with the respective optics. Figure 3 summarizes a comparison of projected ground truths (a), images after reconstruction for the refractive lens (b), hyperboloid (c), and the broadband end-to-end meta-optic (d), respectively. Further raw captures and images after specific operations, as well as comparison to other meta-optics, are further discussed in the Supplementary Information. To recover the image purely based on a physical forward model, we employ here a conventional Wiener deconvolution and

denoising[51] for captures. These were the same for the different optics, while specific parameters were adjusted to yield high-quality imaging.

Under these conditions, the broadband meta-optic provides overall imaging quality on par with a refractive lens, with details and color contrasts accurately captured. Further details of an image (Fig. 2e) are shown in Fig. 2f and Fig. 2g for the refractive lens and the broadband meta-optic, respectively, which highlight the specific shortcomings of each system. Although it captures all colors and mid to large image features, fine structures such as the individual petals of a rose appear more blurred, compared to those of the refractive lens. In contrast, towards large field angles (>10°) the meta-optic provides clearer image features as compared to those of the refractive lens. This enhanced performance at larger field angles is a direct consequence of the more confined PSF of the meta-optic compared to the refractive lens, as shown in Fig. 2.

While the broadband meta-optic captures image details of all colors, the hyperboloid meta-optic is not suitable for generalized scenarios as only partial color information is captured, particularly well seen in the top row images. Although recent works have investigated neural back ends to reconstruct full-color images[41,42], we find that, with results collated in the Supplementary Information, for a large variety of scenes, the hyperboloid is not suitable, making this approach strongly scenario-dependent. We again emphasize that the computational method used here is deliberately based on Wiener deconvolution and is, therefore, fully agnostic to the imaging scene as it only relies on the beforehand measured PSF. We also note that images captured with narrowband hyperboloids and neural back-ends in other works are largely sparse and have less color variation, which simplifies the reconstructions (further discussed in the Supplementary Information).

Towards consumer application scenarios, we further demonstrate the capability of broadband imaging for real-world scenes, as, for example, shown in Fig. 3(h), prepared to contain strong color and detail variations. Images after computation are shown in (i) and (j) for the meta-optic and the refractive lens, respectively, with specific details zoomed in. We find that the broadband MO captures the visible spectrum well, with similar detail close to the performance of the refractive lens. While the image quality is on par for small field angles, we observe that towards larger field angles, the meta-optic, in fact, outperforms the refractive lens, as image details are still recovered in the capture. This can be particularly well observed in the details, shown in Fig. 3i and j. We note that mismatches in color between ground truths and the reconstructed images of the meta-optic and the refractive lens capture occur due to differences in the computational reconstruction, where hues may slightly differ. Nevertheless, colors (RGB) are accurately assigned.

Video-rate imaging

Furthermore, we demonstrate that the meta-optic is suitable for high frame rate captures, as required for broadband video capture. Frames of videos, after reconstruction are shown in Fig. 3k–m, while the full video can be found in the Supplementary Material. In the first video (Supplementary Movie 1 – captured under room light, 5 MPix, captured with an exposure time of 90 ms, and frame rate of ~11 fps), a person is shown jumping in front of the same scene as Fig. 3h, with frames recording movements of the person, mid-jump and with recognizable features on their trousers. In the second video (Supplementary Movie 2 – captured under room light, 5 MPix, captured with an exposure time of 5 ms and additional gain, and frame rate of ~19 fps), a person is shown flipping a coin, whereas the momentary position of the coin mid-air is captured. In the third video (Supplementary Movie 3 – captured under daylight, 5 MPix, captured with an exposure time of 5 ms and frame rate of ~19 fps), we demonstrate the bouncing of a colorful ball, even capturing momentary deformations of the ball

as it is thrown. We note that a black halo appears around the bouncing ball, likely due to non-uniform illumination conditions, which becomes more pronounced during the computational post-processing. This, however, could be removed with further improvement in the computational backend.

Imaging performance with neural backend

By comparing Fig. 3h and i, it becomes clear that while the broadband meta-optic captures color and scene details, it lacks the vibrant image quality achievable with state-of-the-art digital systems, such as smartphone cameras. Thus, to fully leverage the benefit of a computational backend, we further augment the meta-optic with a learned reconstruction method. For advanced and spatially varying aberration correction, and better noise reduction, we designed a probabilistic diffusion-based neural network. To ensure the viability of the specific architecture for imaging under arbitrary conditions (ambient conditions and scene independence), we evaluate the method with a co-axial paired image capture system, schematically shown in Fig. 4a. A beam splitter redirects 30% of light to a compound lens camera, while 70% of light is transmitted to a meta-optic camera. Both imaging systems share the same field of view, which ensures that reconstruction algorithms can be trained on arbitrary scenes. Details on reconstruction architecture and training are given in the Supplementary Information and Methods.

In Fig. 4b, we directly compare ground truth captures (obtained via the compound lens imager), images reconstructed with a physics-based inverse filter, and the learned backend. We note that the presented images were not part of the training set but were captured for verification of the approach. The learned probabilistic diffusion model outputs images which are significantly better than compared with the physics-based inverse filter. Particularly, the images yield lower haze, better color accuracy, produce more vivid hues, better noise reduction, account for spatial variance, and non-uniform sensor response. While parts of these factors could be improved as well in the physics-based backend, the probabilistic diffusion-based reconstruction method directly takes these factors into account. To emphasize this aspect, further scene details are presented in zoomed-in sections in Fig. 4(c). More images and details can be found in the Supplementary Information. As such, the broadband meta-optic with the learned backend produces images that are almost on-par with compound lens camera imagers.

Discussion

We demonstrate visible broadband, video-rate imaging with a single, polarization insensitive, 1 cm aperture, f/2, flat meta-optic. By designing a meta-surface in an end-to-end design fashion, we account for the inherent limitations of the flat diffractive optics in tandem with a computational reconstruction to ensure optimized performance within the provided constraints. This allows us to conclusively show how intrinsic chromatic limitations are overcome, and high-quality images are achievable with only a micron-thick diffractive layer. Through comparison with other designs, including the hyperboloid metalens, an EDOF design, and a polychromatic meta-optic, we validate the respective functionalities and how visible broadband imaging capability arises. Specifically, the formation of an extended depth of focus ensures all wavelengths within a defined spectral range are focused on a common plane. While this extends the PSF laterally, the final image quality is recovered through a deconvolution step. This is possible due to the well-balanced PSF across the entire considered spectral range. While this was previously not clear[52], it shows the highest imaging performance in comparison of the considered meta-optic and close to parity with a refractive lens. We provide a full evaluation of the optical performance, and a head-to-head comparison with a refractive element to give a direct
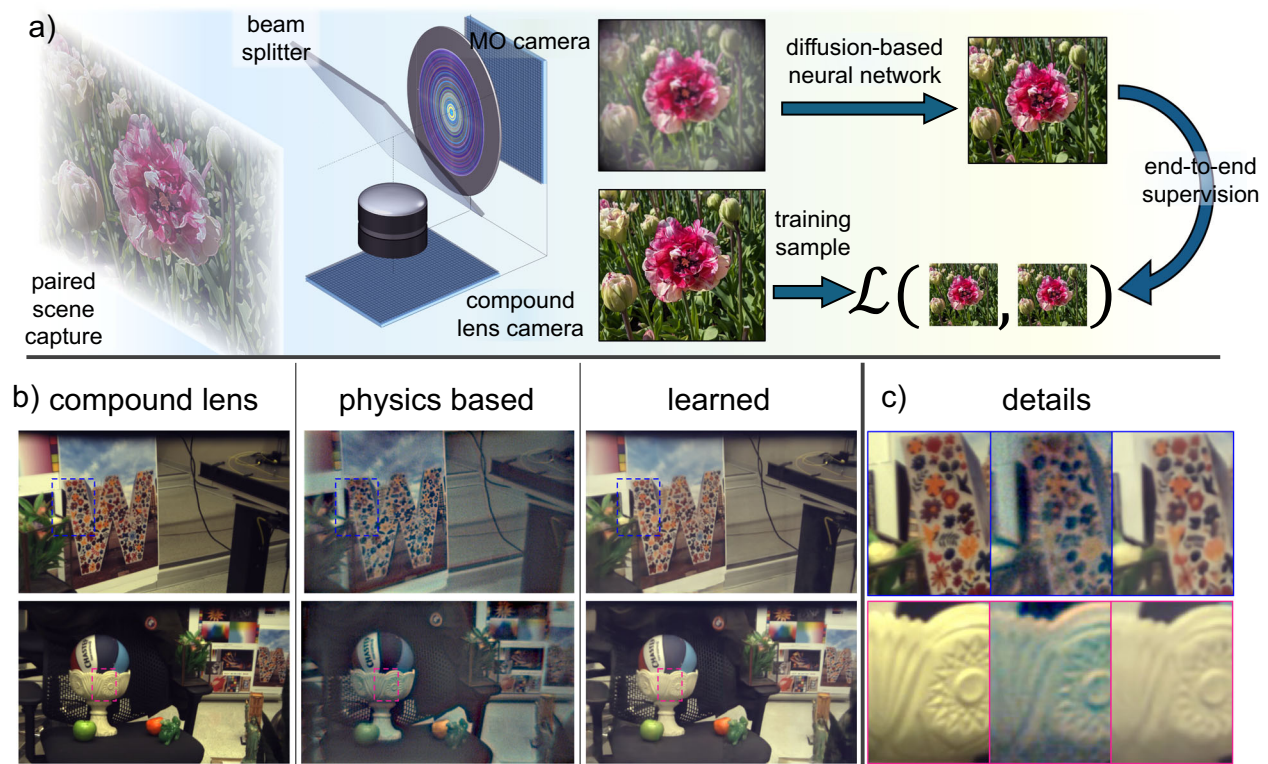
Fig. 4 | Broadband imaging with a learned back end. a Training a neural backend on images from real-life scenes. The same image scenes are captured with a meta-optical camera and a compound lens camera. A diffusion neural network is then trained and used to recover image quality. **b** Comparison of images taken with a compound refractive lens, the broadband meta-optics, and a physics-based inverse filter, and with a learned backend. **c** Zoomed in details of the highlighted boxes in the images are directly compared next to each other.

assessment of how well these optics compare with a refractive lens on the same sensor. Doing so allows us to directly compare against a broadly available benchmark. Moreover, avoiding comparison with other meta-optics of smaller diameters circumvents the pitfall of scaled aberrations. As aberrations scale with the size of an optic, a larger optic will always perform more poorly in terms of its resolving power[48,49]. Beyond that, our system-level comparison takes into account the limitations of the sensor itself, including the sensor MTF and angle of incidence dependence. The fabrication-friendly design is also adoptable and compatible with semiconductor foundries, which recently adopted meta-optic-centered manufacturing approaches and have raised significant funds to focus on large-scale meta-optic production[43-45].

In short, we find on-par imaging performance with a single refractive lens, where we achieve an average MTF contrast after computation of > 30% in a range of 0 − 70 lp/mm, in comparison with an MTF contrast of ~ 50%, for a refractive lens in the same range (after computation). Moreover, we demonstrate improved imaging capabilities using a meta-optic at field angles of 10° and larger. The designed meta-optic is suitable for ambient imaging, and video rate captures with short exposure times in the ms range, which we directly exhibit by capturing the motion of scenes with rapidly moving features. We ultimately achieve on-par performance with compound imagers and demonstrate an approach to implement a learned reconstruction method using probabilistic diffusion models. Overall, this work demonstrates and elucidates, in essence, how broad band imaging in the visible is achievable with an ultra-flat optical element and large aperture (1 cm), and thus challenges the well-trenched belief in the community that broadband imaging is impossible using a large-aperture meta-optics.

Methods

Meta-optic design
Scatterers were designed using the S4 package for rigorous coupled wave analysis[53].

EDOF Design approach
In order to scale up to larger apertures, we reduced the memory requirements by only simulating the center of the field of view. In doing so, we could employ rotationally symmetric image formation models that reduce computationally expensive 2D wave propagation into 1D systems. Coupled together with the RCWA approximation used from our previous work[37] it allowed for fast design of metalenses up to 5 cm in aperture diameter. In terms of design time, the optimization for a single 1 cm aperture metalen takes approximately one hour.

Another difference from our previous work is the sampling of wavelengths. We found that only 3 wavelengths (462, 511, and 606 nm) and using a polynomial basis for the metasurface design did not facilitate a sufficient chromatic correction for larger aperture metasurfaces over the broadband. To remedy this, we instead sampled 1000 wavelengths within the 450–650 nm range, and we used a per-pixel basis for the metasurface design. The per-pixel basis allows each nano-antenna along one radius of the metasurface to vary independently of the other nano-antennas without constraints. The figure of merit (FOM) used is the maximization of focusing energy at the sensor plane for all wavelengths.

End-to-end approach
We use the normal incidence PSF generated by the rotationally symmetric image formation model within the overall end-to-end design pipeline[37]. Specifically, we jointly design the metasurface together with the deconvolution network. The end-to-end optimization begins with

the finetuned PSF obtained with the EDOF approach. We run the optimization process with joint optimization between the network and the metasurface for 1000 iterations.

Fabrication

A ~ 800 nm thick SiN film was deposited on a 300 μm thick quartz wafer using plasma-enhanced chemical vapor deposition (PECVD) in an SPTS PECVD chamber. The wafer was then diced into 1.5 cm squares. After a brief cleaning (in Acetone and IPA) and barrel etch step (O_2, 100 W, 15 s), a positive resist (ZEP 520 A) was spun onto the sample (4k rpm, thickness of ~ 400 nm), followed by baking at 180 °C for 3 min on a hot plate. A conductive polymer layer (DisCharge H2O) was subsequently spun on top at 4k rpm. The resist layer was then patterned using a 100 keV electron beam (JEOL JBX6300FS) at a dose of ~ 300 μC cm^{-2}. The total write time was about 4 1/2 hours. After EBL, the conductive polymer layer was removed in a short IPA bath, and subsequently, the resist was developed at room temperature in Amyl Acetate for 2 min. Subsequently, the sample was descummed in a short barrel etch step (100 W, 15 s). Then, using electron beam evaporation, a layer of ~ 75 nm AlO_x was deposited. The mask was then liftoff overnight in an NMP bath at ~ 100 °C on a hot plate. Subsequently, the SiN layer was etched using a mixture of C_4F_8/SF_6 in an inductively coupled reactive ion etcher (Oxford PlasmaLab System 100). After etching, the chip was subsequently integrated in a 3D-printed holder and mounted in front of the sensor. For SEM imaging, a thin conductive Au/Pd layer was deposited.

Measurements

The refractive lens used for comparison was purchase from Edmund Optics, specifically an uncoated Plano Convex lens with 1 cm diameter, 2 cm focal length.

To measure the PSFs of the optics at various wavelengths, we used a custom-built semi-automated setup, as schematically depicted in Fig. 2a. Light of a broadband continuum source (NKT Photonics SUPERK Fianium FIR-20) is guided through an AOTF (NKT Photonics, SuperK Select) with selectable filter range, then coupled into one end of a single mode fiber (Thorlabs P1-630Y-FC-2). The other fiber end was mounted at a distance of ~ 50 cm away from the optic and placed on a custom-built swing arm, which allows the change of the angle of incidence onto the optics under test while maintaining the same distance. The PSF was then directly captured on the sensor (Allied Vision Pro-Silica GT 1930, with a pixel size of ~ 5.6 μm) while maintaining the same distance from optic to sensor throughout the experiment. The wavelength and captures were automated using a custom script, which ensured that the respective PSF captures were not overexposed.

For MTF measurements (schematic, Fig. 2d), the light of the broadband continuum source was coupled into a Multimode fiber (Thorlabs, 100 μm core size), and subsequently guided through a set of diffusers, and an objective (Mitutoyo, 10X, 0.28 NA) which illuminated a USAF 1951 Target (Thorlabs). The target was captured using the optics, and a tube lens (Thorlabs TTL 180-A) was used to form an image on the sensor (Allied Vision ProSilica GT 1930, with a pixel size of ~ 5.6 μm). The line pair contrast was then calculated using an automated script as discussed in the Supplementary Information.

For image captures of a display, as shown in Fig. 3a–e, a monitor was placed ~ 50 cm in front of the optic under test and a series of images was displayed with an image height/width of ~ 16 cm, corresponding to a horizontal FoV of 20°. Images were captured using an automated script, and a Allied Vision ProSilica GT 1930. Some images were taken from the INRA Holiday set[54]. For image captures under ambient conditions, we prepared a colorful scene as shown in Fig. 3g, the image captured with a Google Pixel 6 A. Other images were captured with a meta-optic or refractive lens and a ZWO ASI183MC Pro camera with a FoV of ~ 30°. We note that for all captures a broadband filter (400 nm – 750 nm) was added in the camera to eliminate undesired IR illumination.

For paired image capture, we built a portable custom capture system with two coaxially aligned cameras, one aligned with the broadband meta optics and one with a compound lens. Both cameras shared the same scene using a 70/30 beam splitter, whereas 70% of light is transmitted to the MO camera, while 30% of light is reflected to the compound lens camera. Both cameras used the same sensor (Allied Vision GT 1930c). We first aligned the imaging system on checkerboard patterns, which ensured that the same image scene would be captured and enable the accurate learning and testing of this imaging system. More details on the paired image capture method can also be found in ref. 39.

Data availability

Data available on request from the authors.

Code availability

All Code is available from the authors upon request.

References

1. Mait, J. N., Euliss, G. W. & Athale, R. A. Computational imaging. *Adv. Opt. Photon.* **10**, 409–483 (2018).
2. Delbracio, M., Kelly, D., Brown, M. S. & Milanfar, P. Mobile computational photography: A tour. *Annu. Rev. Vis. Sci.* **7**, 571–604 (2021).
3. Suo, J. et al. Computational imaging and artificial intelligence: The next revolution of mobile vision. *Proceedings of the IEEE* **111**, 1607–1639 (2023).
4. Neshev, D. N. & Miroshnichenko, A. E. Enabling smart vision with metasurfaces. *Nat. Photon.* **17**, 26–35 (2023).
5. Hu, J., Bandyopadhyay, S. Liu, Y. Shao, L. A review on metasurface: From principle to smart metadevices. *Front. Phys.* **8**, https://doi.org/10.3389/fphy.2020.586087 (2021).
6. Pan, M. et al. Dielectric metalens for miniaturized imaging systems: progress and challenges. *Light Sci. Appl.* **11**, 195 (2022).
7. Kuznetsov, A. I. et al. Roadmap for optical metasurfaces. *ACS Photonics* **11**, 816–865 (2024).
8. An, J. et al. Slim-panel holographic video display. *Nat. Commun.* **11**, 5568 (2020).
9. Fang, X., Ren, H. & Gu, M. Orbital angular momentum holography for high-security encryption. *Nat. Photonics* **14**, 102–108 (2020).
10. Lee, G.-Y. et al. Metasurface eyepiece for augmented reality. *Nat. Commun* **9**, 4562 (2018).
11. Colburn, S. & Majumdar, A. Metasurface generation of paired accelerating and rotating optical beams for passive ranging and scene reconstruction. *ACS Photonics* **7**, 1529–1536 (2020).
12. Guo, Q. et al. Compact single-shot metalens depth sensors inspired by eyes of jumping spiders. *Proc. Natl. Acad. Sci. USA* **116**, 22959–22965 (2019).
13. Lin, Z. et al. End-to-end metasurface inverse design for single-shot multi-channel imaging. *Opt. Express* **30**, 28358–28370 (2022).
14. Rubin, N. A. et al. Matrix Fourier optics enables a compact full-Stokes polarization camera. *Science* **365**, eaax1839 (2019).
15. Shen, Z. et al. Monocular metasurface camera for passive single-shot 4D imaging. *Nat. Commun.* **14**, 1035 (2023).
16. Qin, J. et al. Metasurface micro/nano-optical sensors: Principles and applications. *ACS Nano* **16**, 11598–11618 (2022).
17. Intaravanne, Y. & Chen, X. Recent advances in optical metasurfaces for polarization detection and engineered polarization profiles. *Nanophotonics* **9**, 1003–1014 (2020).
18. Faraji-Dana, M. et al. Compact folded metasurface spectrometer. *Nat. Commun.* **9**, 4196 (2018).
19. Fröch, J. E. et al. Dual band computational infrared spectroscopy via large aperture meta-optics. *ACS Photonics* https://doi.org/10.1021/acsphotonics.2c01017 (2022).
20. Wang, R. et al. Compact multi-foci metalens spectrometer. *Light Sci. Appl.* **12**, 103 (2023).

21. Yang, Z., Albrow-Owen, T., Cai, W. & Hasan, T. Miniaturization of optical spectrometers. *Science* **371**, eabe0722 (2021).
22. Wei, K. et al. Spatially varying nanophotonic neural networks. *Science Advances* **10**, eadp0391 (2024).
23. Zheng, H. et al. Meta-optic accelerators for object classifiers. *Sci. Adv.* **8**, eabo6410 (2022).
24. Huang, L. et al. Photonic advantage of optical encoders. *Nanophotonics* **13**, 1191–1196 (2024).
25. Chen, M. K., Liu, X., Sun, Y. & Tsai, D. P. Artificial intelligence in meta-optics. *Chem. Rev.* **122**, 15356–15413 (2022).
26. Wirth-Singh, A. et al. Compressed meta-optical encoder for image classification. *Advanced Photonics Nexus* **4**, 026009–026009 (2025).
27. Arbabi, E., Arbabi, A., Kamali, S. M., Horie, Y. & Faraon, A. Multi-wavelength polarization-insensitive lenses based on dielectric metasurfaces with meta-molecules. *Optica* **3**, 628–633 (2016).
28. Huang, L., Colburn, S., Zhan, A., Majumdar, A. Full-color metaoptical imaging in visible light. *Adv. Photon. Res.* **3**, 2100265 (2022).
29. Presutti, F. & Monticone, F. Focusing on bandwidth: achromatic metalens limits. *Optica* **7**, 624–631 (2020).
30. Engelberg, J. & Levy, U. Achromatic flat lens performance limits. *Optica* **8**, 834–845 (2021).
31. Lin, R. J. et al. Achromatic metalens array for full-colour light-field imaging. *Nat. Nanotechnol.* **14**, 227–231 (2019).
32. Wang, S. et al. A broadband achromatic metalens in the visible. *Nat. Nanotech* **13**, 227–232 (2018).
33. Chen, W. T. et al. A broadband achromatic metalens for focusing and imaging in the visible. *Nat. Nanotech* **13**, 220–226 (2018).
34. Chen, W. T., Zhu, A. Y. & Capasso, F. Flat optics with dispersion-engineered metasurfaces. *Nat. Rev. Mater.* **5**, 604–620 (2020).
35. Fröch, J. E. et al. Real time full-color imaging in a Meta-optical fiber endoscope. *eLight* **3**, 13 (2023).
36. Hu, Y. et al. Asymptotic dispersion engineering for ultra-broadband meta-optics. *Nat. Commun.* **14**, 6649 (2023).
37. Tseng, E. et al. Neural nano-optics for high-quality thin lens imaging. *Nat. Commun.* **12**, 6493 (2021).
38. McClung, A., Samudrala, S., Torfeh, M., Mansouree, M. & Arbabi, A. Snapshot spectral imaging with parallel metasystems. *Sci. Adv.* **6**, eabc7646 (2020).
39. Chakravarthula, P. et al. Thin on-sensor nanophotonic array cameras. *ACM Trans. Graph.* **42**, 249:1–249:18 (2023).
40. Baranikov, A. V. et al. Large Field-of-View and Multi-Color Imaging with GaP Quadratic Metalenses. *Laser & Photonics Reviews* **18**, 2300553 (2024).
41. Maman, R., Mualem, E., Mazurski, N., Engelberg, J. & Levy, U. Achromatic imaging systems with flat lenses enabled by deep learning. *ACS Photonics* **10**, 4494–4500 (2023).
42. Dong, Y. et al. Achromatic single metalens imaging via deep neural network. *ACS Photonics* **11**, 1645–1656 (2024).
43. Egede Johansen, V. et al. Nanoscale precision brings experimental metalens efficiencies on par with theoretical promises. *Commu Phys.* **7**, 1–7 (2024).
44. Williams, B. R. et al. "Metalenses for visible wavelengths: NIL volume manufacturing" In *High Contrast Metastructures XII* (SPIE, 2023).
45. Williams, B. R. et al. "NIL enabled mass production of visible meta-optics". In *Advanced Fabrication Technologies for Micro/Nano Optics and Photonics XVII* (SPIE, 2024).
46. Xiao, X. et al. Large-scale achromatic flat lens by light frequency-domain coherence optimization. *Light Sci. Appl.* **11**, 323 (2022).
47. Meem, M. et al. Large-area, high-numerical-aperture multi-level diffractive lens via inverse design. *Optica* **7**, 252–253 (2020).
48. Lohmann, A. W. Scaling laws for lens systems. *Appl. Opt.* **28**, 4996–4998 (1989).
49. Brady, D. J. & Hagen, N. Multiscale lens design. *Opt. Express* **17**, 10659–10674 (2009).
50. Torralba, A. & Oliva, A. Statistics of natural image categories. *Network* **14**, 391 (2003).
51. Mäkinen, Y., Azzari, L. & Foi, A. Collaborative filtering of correlated noise: Exact tansform-domain variance for improved shrinkage and patch matching. *IEEE Trans. Image Process.* **29**, 8339–8354 (2020).
52. Engelberg, J. & Levy, U. Generalized metric for broadband flat lens performance comparison. *Nanophotonics* **11**, 3559–3574 (2022).
53. Liu, V. & Fan, S. S4: A free electromagnetic solver for layered periodic structures. *Comput. Phys. Commun.* **183**, 2233–2244 (2012).
54. Jegou, H., Douze, M., & Schmid, C. in *Computer Vision – ECCV 2008* (2008).
55. Colburn, S., Zhan, A. & Majumdar, A. Metasurface optics for full-color computational imaging. *Sci. Adv.* **4**, eaar2114 (2018).
56. Chen, W. T., Zhu, A. Y., Sisler, J., Bharwani, Z. & Capasso, F. A broadband achromatic polarization-insensitive metalens consisting of anisotropic nanostructures. *Nat. Commun.* **10**, 355 (2019).

Acknowledgements

Author contributions

F.H. and A.M. conceived the idea. P.C. designed the end-to-end meta-optics with help from E.T. under the guidance of F.H. and A.M. S.C., and A.Z. designed the EDOF meta-optics. J.E.F. fabricated all meta-optics with assistance from F.M., A.W. Q.A.A.T., and Z.H. and guidance from K.F.B. and A.M. J.E.F. performed all characterization of meta-optics and conducted imaging experiments with Wiener based filtering including Figs. 1 – 3. P.C. developed the neural backend for improved imaging and conducted experiments with the co-axial camera, with assistance from J.S. and E.T., with results presented in Fig. 4. J.E.F. and P.C. lead analysis and interpretation of data, with discussions with all authors. J.E.F., P.C., F.H., and A.M. wrote the manuscript with input from all authors.

Competing interests

Additional information